4、 外语能力证书

全国大学英语四级考试(CET4)成绩报告单

姓　　名：周飞

证件号码：[redacted]

学　　校：安徽农业大学

笔试成绩

准考证号：[redacted]

总　　分：444

听　　力：155

阅　　读：179

写作和翻译：110

考试时间：2020年12月

5、 学术能力证明材料

Materials Today Chemistry 40 (2024) 102198

Contents lists available at ScienceDirect

Materials Today Chemistry

journal homepage: www.journals.elsevier.com/materials-today-chemistry/

Morphology-dependent metal-organic frameworks via solvent and Co ion effect for high performance battery-supercapacitor hybrid device

Fei Zhou, Guangjun Liu, Changfu Zhuang, Ying Wang, Di Tian *

Key Laboratory of National Forestry and Grassland Administration on Highly-Efficient Utilization of Forestry Biomass Resources in Southwest, Southwest Forestry University, Kunming, 650024, PR China

ARTICLE INFO

Keywords:
MOFs
Battery-supercapacitor hybrid device
Solvent effect
Co ion effect

ABSTRACT

MOFs have been widely recognized in battery-supercapacitor hybrid devices. Here, the electrochemical performance of Ni MOF as a battery-type material was primarily improved by morphological engineering based on solvent and Co ions. Varying the solvent type, solvent ratio, and Ni/Co ratio, NiCo(1:0.5)MOF H_2O showed the largest specific capacitance of 1225.56 F g^{-1} (specific capacity of 551.50 C g^{-1}) at 0.5 A g^{-1}, owing to its largest specific surface and good redox activity caused by the difference in the solvent solubility, solvent polarity and coordination ability of metal ions. Furthermore, a solid-state battery-supercapacitor hybrid device was assembled, serving NiCo(1:0.5)MOF H_2O and active carbon material obtained from bamboo as the positive and negative electrodes, separately. At a power density of 750.00 W kg^{-1}, this device emerged with a large energy density of 108.96 Wh kg^{-1}. After 5000 cycles, it can maintain 89.09 % of the initial value. Notably, this device could furnish energy for the LED emitting, reflecting a giant application potential.

1. Introduction

Metal-organic frameworks (MOFs), a porous crystalline hybrid material, are assembled by organic ligands and metal ions. Their diversities of structure and composition endow MOFs with the features of rich active sites, adjustable pore structure, large specific surface area, and flexible chemical functionality, leading to a wide application field, such as energy storage, catalysis, chemical sensing, gas separation, pollutant adsorption, etc [1–3]. Recently, battery-supercapacitor hybrid (BSH) devices have been of great interest to researchers. Integrating battery-type material and capacitive material in one device to make the best of their respective advantages in high energy and power densities [4,5]. In general, carbon materials as capacitive materials have realized commercialized production because of their fast rate performance, high stability as well as low cost. Significantly, battery-type materials with strong charge storage ability are desired to construct a high-performance BSH.

MOFs belong to one of the battery-type materials [6–9]. In addition to directly serving as an electrode material, it can also act as a precursor material or template material for converting into porous metal oxides/sulfides/phosphides [10–12]. Compared to the latter, the former has a simpler synthesis route. The electrochemical performance of MOFs is mostly determined by their specific surface areas along with redox activity. Metal centers such as cobalt, nickel, and iron can provide superb redox activities. Meanwhile, bimetallic organic frameworks often possess higher redox activities [13,14]. Moreover, the crystal structure and morphology of MOFs primarily dictate their specific surface areas.

The crystal structure and morphology of MOFs can be regulated by growth time and speed, molar ratio of reactants, pH, solvent, growth temperature, surfactants, etc [15–19]. Among them, solvent not only coordinates with metal ions but also serves as a structure-directing agent and a reaction medium to affect the crystal structure and morphology, which stem from the difference in the solvent polarity, viscosity, deprotonation ability, solubility, molecular sizes, and coordination ability [20–22]. In previous reports, solvent regulation mainly focused on the control of solvent types and ratios. In the meantime, it is not limited to a specific type of MOFs, involving in diverse metal centers and ligands. Han and co-workers [23] have prepared three amino-functionalized bimetal MOFs in different morphologies by a solvent-controlled method, which reached the greatest specific capacitance of 1126.70 F g^{-1} at the current density of 0.5 A g^{-1}. Moreover, MeOH and DMF were used as cosolvents with different volume ratios to modulate the size and morphology of Zn-MOF depending on a weaker template effect [24]. To achieve better energy storage capacity,

* Corresponding author.
E-mail address: 13366023523@swfu.edu.cn (D. Tian).

https://doi.org/10.1016/j.mtchem.2024.102198
Received 24 April 2024; Received in revised form 29 June 2024; Accepted 12 July 2024
Available online 21 July 2024

multi-directional regulation strategies have been enforced in MOFs. For instance, the surfactant effect and solvent effect were employed to effectively regulate the morphology and nano sizes of Ni MOFs and Cu MOFs, resulting in superb specific capacitance and cycling stability [25].

Biomass-derived carbon materials as a typical capacitive material have attracted much interest because of their rich reserves, intrinsic structural characteristics, and renewability. Wherein, bamboo resources with the characteristics of large aspect ratio structure and rapid growth, are regarded as a promising precursor [26,27]. However, its development is hindered by its limited specific surface areas, whose effective solution is KOH activation. KOH-activated bamboo-based carbon materials have a wide range of applications in many fields. For example, Yu and coworkers [28] designed a bamboo-derived activated carbon for high CO_2 adsorption. In 2006, a KOH-activated bamboo-based carbon was reported, which exhibited a good capacitive performance [29].

Herein, MOFs based on BDC ligands were fabricated by a facile solvothermal method. Morphological engineering dominated by solvent effects as well as metal ions regulation was conducted to improve its electrochemical performance. As a result, NiCo(1:0.5)MOF H_2O exhibited the largest specific capacitance of 1225.56 F g^{-1} (specific capacity of 551.50 C g^{-1}) at 0.5 A g^{-1}, emerging battery-type characteristics as positive electrode. Moreover, the negative electrode was KOH-activated carbon material derived from bamboo. The assembled solid hybrid supercapacitor emerged with a large energy density of 108.96 Wh kg^{-1} when its power density reached 750.00 W kg^{-1}. After 5000 cycles, the capacitance retention of the device is up to 89.09 %, which can support for the LED emitting.

2. Experimental section

2.1. Chemicals and materials

Nickel nitrate hexahydrate ($Ni(NO_3)_2•6H_2O$), N, N-dimethylformamide (DMF), N, N-dimethylacetamide (DMA), potassium hydroxide (KOH), methanol (MeOH), and ethanol (EtOH), as well as cobalt nitrate hexahydrate ($Co(NO_3)_2•6H_2O$) were purchased from Sinopharm Chemical Reagent Co.; Terephthalic acid (H_2BDC), and polytetrafluoroethylene (PTFE) were purchased from Aladdin.

2.2. Preparation of Ni-MOF S (S = DMA, DMF, EtOH, MeOH, H_2O)

$Ni(NO_3)_2•6H_2O$ (0.582 g) was dissolved in 15 mL DMF to obtain solution A. H_2BDC (0.084 g) was dissolved in 10 mL DMF to get solution B. A and B were mixed in the autoclave and reacted at 120 °C for 16 h. The sample was collected by centrifuges, dried at 80 °C for 12 h in a vacuum oven, and named Ni MOF. When 1 mL DMA, 1 mL DMF, 1 mL EtOH, 1 mL MeOH, H_2O (1–4 mL) were added in solution B, the obtained samples were called Ni-MOF DMA, Ni-MOF DMF, Ni-MOF EtOH, Ni-MOF MeOH, Ni-MOF H_2O, Ni-MOF H_2O2, Ni-MOF H_2O3, Ni MOF H_2O4, respectively.

2.3. Preparation of NiCo(x:y)MOF H_2O (x:y = 1:0.25, 1:0.5, 1:0.75 and 1:1)

Similarly, NiCo(x:y)MOF H_2O (x:y = 1:0.25, 1:0.5, 1:0.75 and 1:1) were prepared by the above solvothermal reaction process except for the addition of $Co(NO_3)_2•6H_2O$. Under the same reaction conditions, the mole ratio of $Ni(NO_3)_2•6H_2O/Co(NO_3)_2•6H_2O$ was 1: 0.25, 1: 0.5, 1: 0.75, and 1: 1, which were dissolved into solution A. The obtained samples were marked as NiCo(1:0.25)MOF H_2O, NiCo(1:0.5)MOF H_2O, NiCo(1:0.75)MOF H_2O, and NiCo(1:1)MOF H_2O, respectively.

2.4. Preparation of BAC

The bamboo powder was carbonized at 500 °C in a tube furnace under nitrogen protection and held for 1.5 h (5 °C min^{-1}). The resulting carbon materials were immersed in 6 mol L^{-1} KOH for 4 h and then dried at 105 °C for 12 h. The obtained material was carbonized at 600 °C for 1.5 h. The resulting material was named as BAC until neutrality with 1 mol L^{-1} of HCl and deionized water.

3. Result and discussion

Fig. 1a shows the synthetic route and crystal structure of MOFs. MOFs with various morphologies were achieved via a facile solvothermal route under the solvent effect and metal ion effect. In detail, the morphological difference in Ni MOF mainly relies on the influence of solvent polarity and solubility as well as the coordination ability between metal ions and H_2BDC. On the one hand, solvent polarity acts as a major factor in the amount of deprotonated H_2BDC [30,31]. A faster deproton rate is achieved in DMF, resulting in a smaller size of MOFs. Among the solvents, H_2O possesses the highest affinity to Ni^{2+}, and smaller solubility for H_2BDC, so a high interfacial tension will prohibit the nucleation of MOFs [32]. Compared with Ni ions, Co ions with weaker coordination ability than Ni ions will slow down or even stop the growth of crystals [33].

XRD and FTIR analyses are provided to explore the crystal structure of the samples. From Fig. 1b, Ni-MOF MeOH exhibits strong diffraction peaks at around 8.79° and 15.52°, followed by a series of weaker peaks between 20.26° and 50.14°, in accordance with the previously reported MOF [34]. Differently, Ni-MOF S (S = DMA, DMF, and EtOH) present one obvious diffraction peak at 8.38°, due to their faster deproton rate than others. Ni-MOF H_2O and Ni-MOF MeOH possess similar crystal structures (Fig. 1c). Because H_2O possesses the highest affinity to Ni^{2+}, and smaller solubility for H_2BDC, the increased water plays a negative role in the growth of its crystal structure, leading to the decreased crystallinity of Ni MOF with increasing water content. Meanwhile, some new diffraction peaks appear, but the position of the main peak has no obvious shift, which is associated with the introduction of varying degrees of water molecules into their crystal structure [35]. When Co ions were added in MOFs, there was also crystal structure transformation during 14.91–20.18° in Fig. 1d. From the magnified XRD pattern of NiCo (1:0.5)MOF, there are two peaks at around 8.50°, revealing the generation of new crystal phases caused by Co ions. Compared with the low Co content, The position of the main peak for high Co content shifts towards a higher degree, suggesting the lattice contraction is caused by the smaller radius of cobalt compared to nickel. In Fig. S1, the weak peak near 44.18° in the XRD pattern of BAC belongs to the (100) side of amorphous carbon, and its wide peak near 22.42° belongs to the (002) side of graphitic carbon [36]. In order to further explore the differences in crystal structure, FTIR spectra are provided in Fig. 1e–g. In detail, the symmetric and asymmetric stretching patterns of –COO groups in terephthalic acid are detected at 1378.00 and 1584.00 cm^{-1}, separately, whose difference suggests that two oxygen atoms in –COO groups are coordinated to nickel. The band corresponded to a typical stretching vibration of intramolecular hydrogen bonding is located at 3525.00 cm^{-1}, suggesting that water molecules appear in the polymer structure [37,38]. The characteristic absorption peaks located at 682.76 cm^{-1} are indexed to the Co–O bond [39], ensuring the successful coordination of Co ions with H_2BDC. Furthermore, the results are in line with that in XRD, suggesting the existence of Ni–Co bimetallic organic frameworks. The similar coordination modes between Co or Ni ion with H_2BDC are observed in other similar peaks.

SEM images display the morphological characteristics of MOFs. The morphology of Ni-MOF DMF (Fig. 2a) shows a relatively smooth sphere in shape, whose diameter ranges from 1 μm to 3 μm. From Fig. 2b and c, Ni-MOF DMA and Ni-MOF EtOH also display similar spherical shapes, but a rougher surface and varying degrees of stacking. Differently, obvious nanosheets appear and gather together for Ni-MOF MeOH in Fig. 2d, forming a hydrangea-like morphology. Ni-MOF H_2O (Fig. 2e) presents a layered stacking morphology covered with nanosheets. Compared with Ni-MOF H_2O, the morphologies of samples in Fig. 2f–h

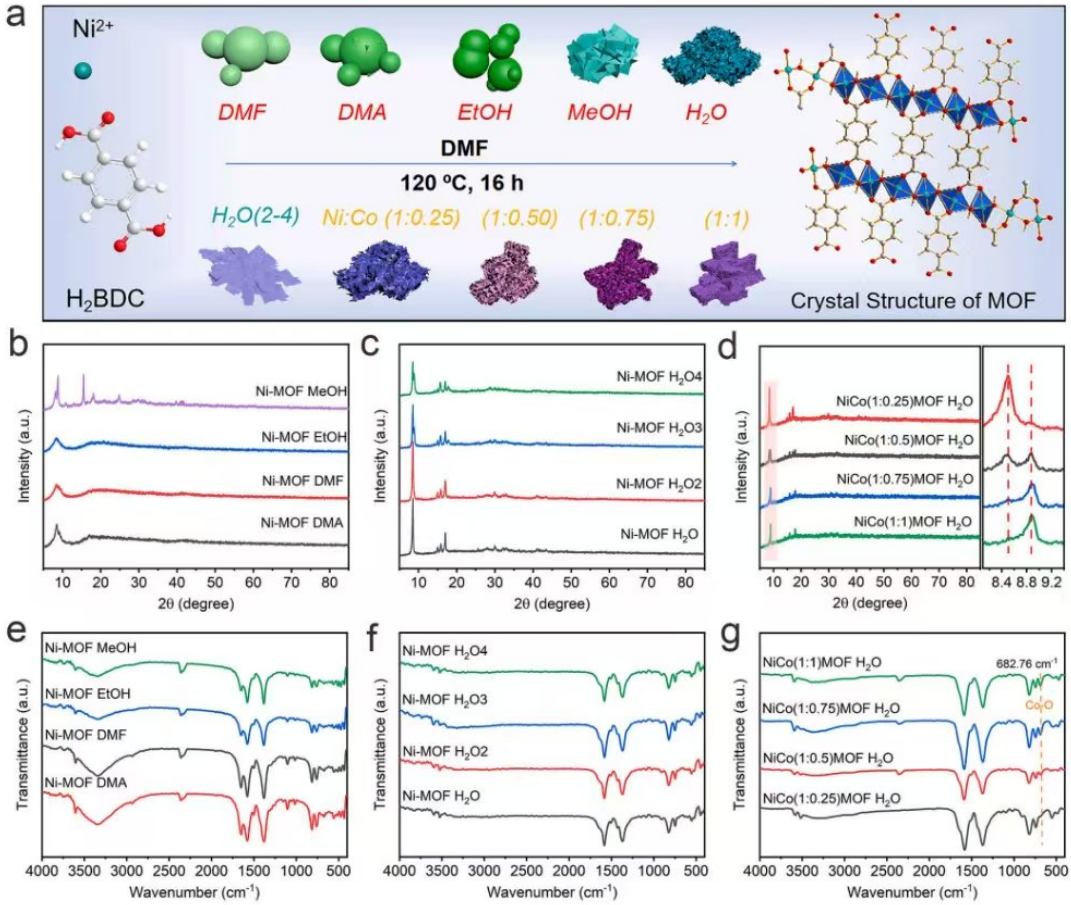

Fig. 1. (a) Synthetic routes and crystal structure of MOFs. XRD pattern of (b) Ni-MOFs S (S = DMA, DMF, EtOH, MeOH), (c) Ni-MOFs S (S=H_2O, H_2O2, H_2O3, H_2O4), (d) NiCo(x:y)MOF H_2O (x:y = 1:0.25, 1:0.5, 1:0.75 and 1:1); FTIR spectra of (e) Ni-MOFs S (S = DMA, DMF, EtOH, MeOH), (f) Ni-MOFs S (S=H_2O, H_2O2, H_2O3, H_2O4), (g) NiCo(x:y)MOF H_2O (x:y = 1:0.25, 1:0.5, 1:0.75 and 1:1).

shows obvious differences. The nanosheets with a thickness of 30 nm are radially stacked together, which suggests that the volume of water added ranging from 2 mL to 4 mL does not have a major influence on the morphology of the material. On the whole, Ni-MOF S (S=H_2O and MeOH) show larger sizes than Ni-MOF S (S = DMA, DMF, and EtOH), owing to the slower nucleation rate caused by the slower deproton rate. Besides, due to H_2O with high affinity to Ni^{2+} and small solubility for H_2BDC, a high interfacial tension will prohibit the nucleation of MOFs. Therefore, MOFs tend to grow in a specific direction. For the NiCo (1:0.25)MOF H_2O, crosslinked nanosheets are observed in Fig. 2i. From Fig. 2j–l, MOFs exhibit a coral-like morphology as a whole. Compared with Ni ions, Co ions with weaker coordination ability than Ni ions slow down or even stop the growth of crystals, so their surface becomes smoother and smoother when the mole ratio of Ni/Co decreases from 1:0.25 to 1:1. NiCo(1:0.5)MOF with a villous surface covered by smaller sized nanosheets can expose more active sites. The SEM images of BAC (Fig. S2) reflect that the bamboo powder derived carbon presents a layered stacking, whose surface is covered with nanosheets after activation.

The morphology and composition of samples were analyzed using TEM images and their EDX spectra. The TEM image of NiCo(1:0.5)MOF H_2O shown in Fig. 3a reflects the successful coordination of metal ions with ligands. Meanwhile, their shape in elemental mapping (Fig. 3b–e) is similar to that in the TEM image, suggesting that Ni, Co, O, and C elements are evenly dispersed in the whole sample. Fig. 3f shows that NiCo(1:0.5)MOF H_2O is composed of Ni, Co, O, and C. The ratio of Ni and Co elements in NiCo(1:0.5) MOF H_2O is 4.56, which is demonstrated in Table S1. XPS spectra are offered to further study their composition and element valence. From Fig. 3g, Ni, Co, O, N, and C signals appear in the full spectrum of NiCo(1:0.5)MOF H_2O. The XPS spectrum of the Co 2p region (Fig. 3h) is decomposed into four peaks. The peaks located at 781.48 and 797.68 eV are assigned to Co $2p_{3/2}$ and Co $2p_{1/2}$, while the two broad peaks at 802.38 and 786.28 eV belong to the vibrational satellite peaks of $Co2p_{1/2}$ and $Co2p_{3/2}$, respectively. This result shows the characteristic spectral band of Co^{2+} [40]. Fig. 3i shows the XPS spectrum of Ni 2p, its binding energies at 856.38 and 873.98 eV belong to Ni $2p_{3/2}$ and Ni $2p_{1/2}$, while the two peaks at other positions correspond to their vibrational satellite peaks. These findings present the characteristic spectral bands of Ni^{2+} [41]. Therefore, Ni^{2+} and Co^{2+} dominate in this material. For C1s (Fig. S3a), the two peaks at 288.68 and 284.88 eV are ascribed to the C=O and C–C/C=C bonds [42]. While in O1s (Fig. S3b), the peaks at 532.68 and 531.78 eV are ascribed to C–OH bonds and metal-oxygen bonds (M-*O*-M) [23], respectively.

Pore-size distribution curves and N_2 adsorption-desorption isotherms are employed to evaluate the characteristics of pore structure. The shapes of isotherms in Fig. S4a match with the typical IV isotherm. At medium relative pressure, the hysteresis loop with a vertical tail at about P/P_0 = 1.0 appears, revealing the existence of mesopores and

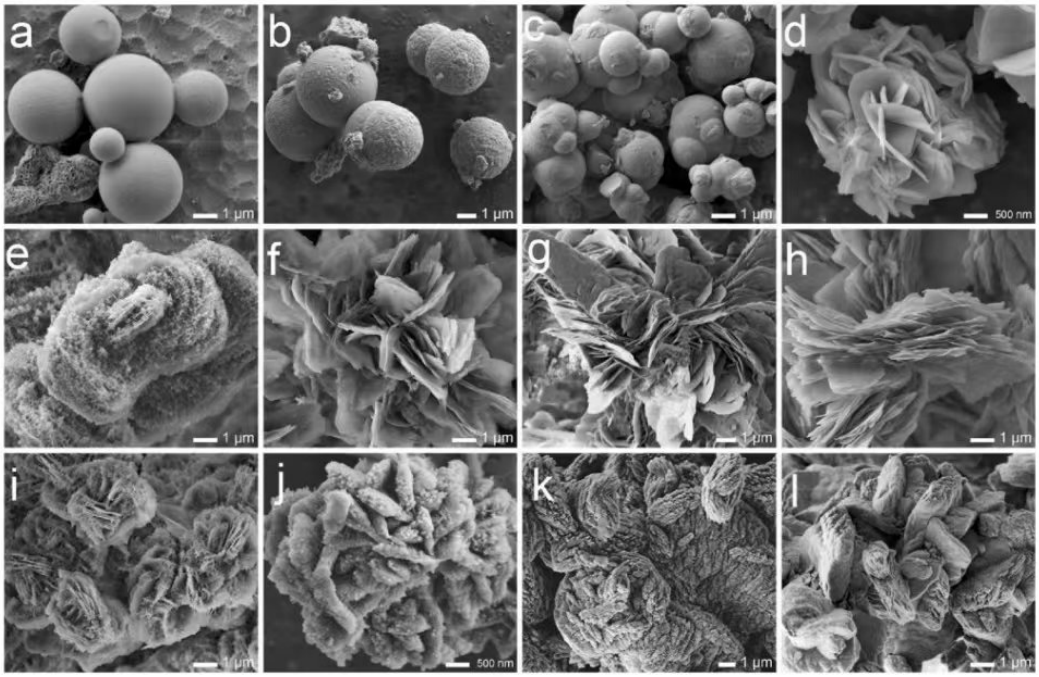

Fig. 2. SEM images of Ni-MOF S (S= (a) DMF, (b) DMA, (c) EtOH, (d) MeOH, (e) H_2O, (f) H_2O2, (g) H_2O3, (h) H_2O4), (i) NiCo(1:0.25)MOF H_2O, (j) NiCo(1:0.5)MOF H_2O, (k) NiCo(1:0.75)MOF H_2O, (l) NiCo(1:1)MOF H_2O.

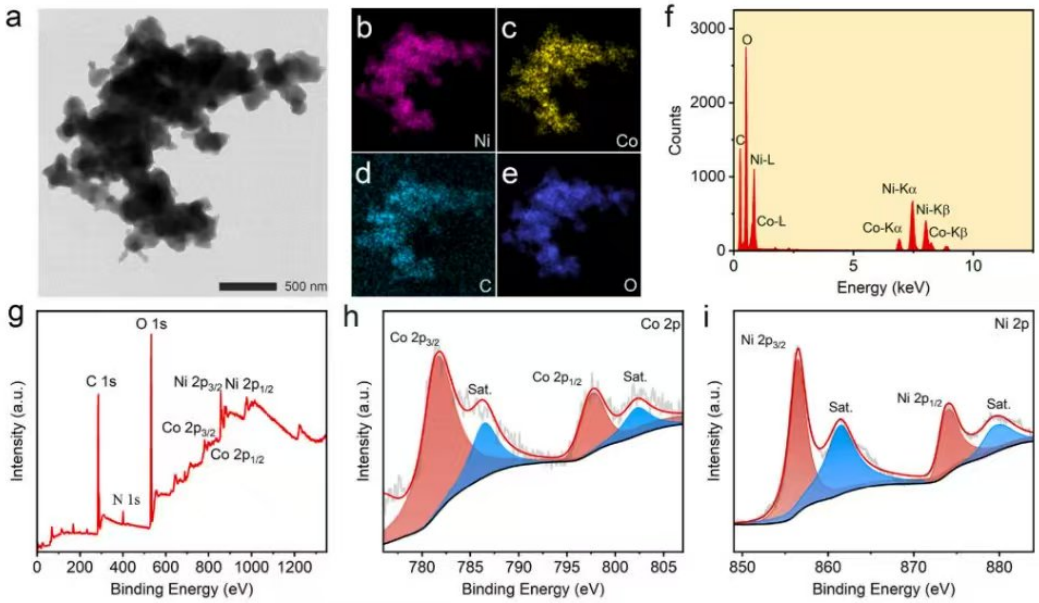

Fig. 3. (a) TEM image and its elemental mapping for (b) Ni, (c) Co, (d) C, and (e) O, (f) EDX spectrum, (g) XPS full spectrum, XPS spectrum of (h) Co 2p and (i) Ni 2p of NiCo(1:0.5)MOF H_2O.

macropores for NiCo(1:0.5)MOF H_2O [43,44]. Fig. S4b reflects that mesopores with an aperture of 10–20 nm dominate. Based on the BET method (Fig. 4a), NiCo(1:0.5)MOF H_2O exhibits the greatest specific surface area of 84.24 $m^2\ g^{-1}$, which may contribute to the exposure of more active sites in KOH. Based on the morphology and structural characterization of MOFs, the specific surface areas are related to their specific morphology. In Fig. 4b, ICP-OES measurements of NiCo(x:y) MOF H_2O (x:y = 1:0.25, 1:0.5, 1:0.75 and 1:1) are offered. The mole ratios of Ni/(Ni + Co) in NiCo(x:y)MOF H_2O (x:y = 1:0.25, 1:0.5, 1:0.75 and 1:1) are calculated to be 92.64, 87.34, 78.29 and 74.57 %,

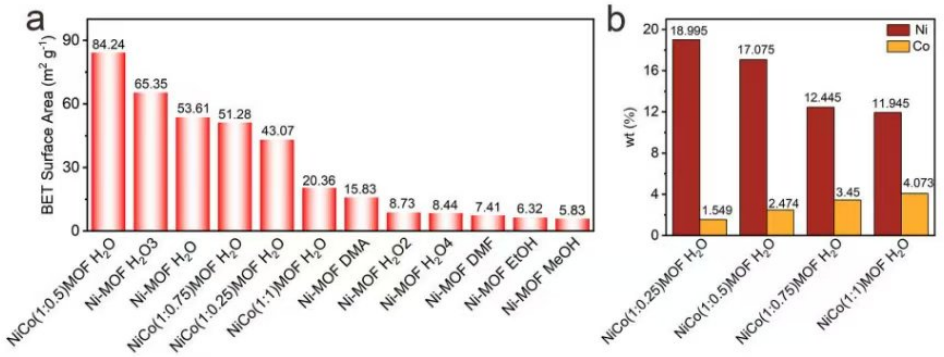

Fig. 4. (a) BET results of different samples. (b) ICP-OES measurements of NiCo(x:y)MOF H_2O (x:y = 1:0.25, 1:0.5, 1:0.75 and 1:1).

respectively, which are lower than its added ratio. These results suggest that Ni is easier to coordinate with terephthalic acid than Co under this synthetic condition.

In a three-electrode system, CV, GCD, and EIS curves are measured to evaluate the electrochemical performance of the samples. First, the type and amount of solvents are discussed. The CV curves (Fig. 5a) of Ni-MOFs S (S = DMA, DMF, EtOH, MeOH, H_2O) show clear redox peaks, suggesting their battery-like behavior. Among them, Ni-MOFs H_2O delivers the largest areas enclosed by CV curves. GCD curves at 0.5 A g^{-1} are shown in Fig. 5b, the specific capacitances of Ni-MOFs S (S = DMA, DMF, EtOH, MeOH, H_2O) are 488.89, 476.67, 534.44, 487.78, 886.67 F g^{-1} (the specific capacities are 220.00, 214.50, 240.50, 219.50, 399.00 C g^{-1}). In Fig. 5c, as the amount of water added increases from 1 mL to 4 mL, the shape of the CV curves is consistent with each other, and the specific capacitance based on GCD curves (Fig. 5d) decreases, which indicates that adding 1 mL H_2O to the original synthesis conditions is the optimal condition for enhancing the ability to store electrons. In addition, the GCD curves at 0.5–10 A g^{-1} of Ni-MOFs H_2O are illustrated in

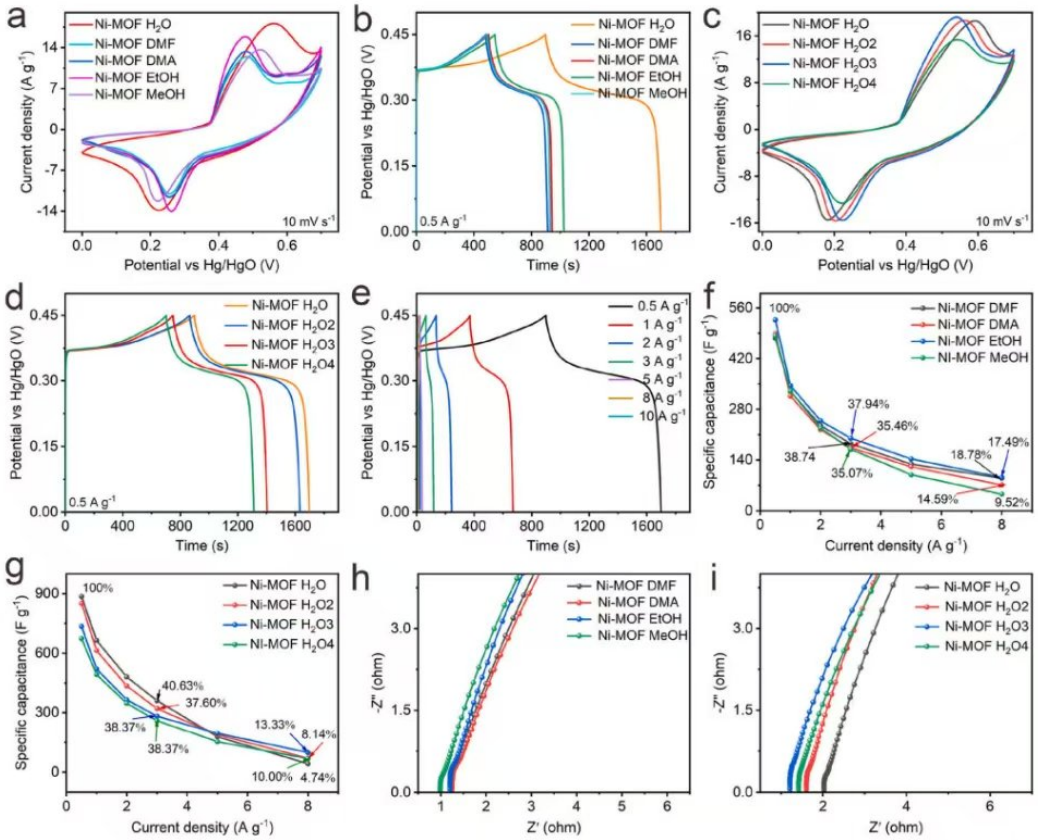

Fig. 5. (a) CV and (b) GCD measurements of Ni-MOF S (S = DMA, DMF, EtOH, MeOH, H_2O), (c) CV and (d) GCD curves of Ni-MOF S (S=H_2O, H_2O2, H_2O3, H_2O4), (e) GCD measurements at diverse current density of NiCo(1:0.5)MOF H_2O, (f) rate performance of (f) Ni-MOF S (S = DMA, DMF, EtOH, MeOH) and (g) Ni-MOF S (S=H_2O, H_2O2, H_2O3, H_2O4), EIS curves of (h) Ni-MOF S (S = DMA, DMF, EtOH, MeOH) and (i) Ni-MOF S (S=H_2O, H_2O2, H_2O3, H_2O4).

Fig. 5e, whose charging and discharging platform correlates with the redox reaction of Ni^{2+}/Ni^{3+}. The rate performance of samples is illustrated in Fig. 5f and g. Among them, when the current density increases from 0.5 A g^{-1} to 8 A g^{-1}, Ni-MOF DMF exhibits the best rate performance: its specific capacitance maintains 18.78 % of initial capacitance, which corresponds to its lower ion diffusion resistance in Fig. 5h. In addition, Ni-MOF H_2O also displays better rate performance than Ni-MOF S (S=H_2O2, H_2O3, H_2O4). As shown in Fig. 5i, the high slope and smaller radius of Ni-MOF H_2O reveal the lower ion transfer impedance and charge-transfer resistance than Ni-MOF S (S=H_2O2, H_2O3, H_2O4), respectively.

Co ions were introduced in Ni-MOF and its mole ratio of Ni to Co was controlled to enhance its electrochemical performance even more. All of the CV curves from Fig. 6a have two redox peaks, which are in good agreement with the redox reactions of Ni^{2+}/Ni^{3+} and Co^{2+}/Co^{3+}. In the basis of GCD curves (Fig. 6b), the specific capacitances of NiCo(x:y)MOF H_2O (x:y = 1:0.25, 1:0.5, 1:0.75 and 1:1) are 981.11, 1225.56, 1124.44, 1085.56 F g^{-1} at 0.5 A g^{-1} (the specific capacities are 441.50, 551.50, 505.99, 488.50 C g^{-1}). The specific capacitances of samples at the current density of 0.5, 1, 2, 3, 5, and 8 A g^{-1} are displayed in Fig. 6c. Among them, NiCo(1:0.25)MOF H_2O emerges with the highest capacitance retention (36.34 %), when the current density becomes 16 times the original. From Fig. 6d, NiCo(1:0.5)MOF H_2O shows the lowest ion diffusion resistance and charge transfer resistance, which results from the high specific surface areas and excellent conductivity from the optimal Ni/Co ratio.

Under the effect of both solvent and Co ions, Ni-MOFs display similar crystal structures and various morphologies. The various morphologies stem from the difference in the solvent solubility, solvent polarity, and coordination ability of metal ions. In addition, an appropriate Ni/Co ratio contributes to favorable redox activity and conductivity. From the perspective of the structure, composition, and electrochemical performance, NiCo(1:0.5)MOF H_2O shows the highest electronic storage capacity, due to the largest specific surface areas as well as the superb electrochemical activities. The larger specific surface areas expose more Co and Ni redox sites to the electrolytes, leading to favorable charges and ions transport.

Considering the superior electrochemical performance of NiCo (1:0.5)MOF H_2O, it was served as the cathode material to build BSH. Meanwhile, a bamboo powder-derived active carbon (BAC) was selected as the negative electrode. So the hybrid supercapacitor device is named NiCo(1:0.5)MOF H_2O//BAC, whose structure diagram is shown in Fig. 7a. The electrochemical test of BAC (Fig. S5) reveals its energy storage mechanism of double electron layer capacitors and electronic storage capacity. According to the specific capacitance of NiCo(1:0.5) MOF H_2O and BAC, their charge balance was conducted. CV (Fig. 7b) and GCD (Fig. 7c) curves of the device are measured within diverse potential windows. When the potential window is 0–1.0, 0–1.1, 0–1.2, 0–1.3, 0–1.4, and 0–1.5 V, its specific capacitance is 18.80, 35.36, 45.83, 52.54, 105.00, and 348.67 F g^{-1}. The maximum specific capacitance arises in 0–1.5 V. As a result, Fig. 7d and Fig. 7e also include the CV at various scan rates and GCD curves at various current densities in the range of 0–1.5 V. The shape of CV curves reflects the hybrid supercapacitor feature. The specific capacitances of the BSH are 348.67, 246.67, 240.80, 213.33, 184.53, and 170.33 F g^{-1} at 1, 2, 3, 5, 8, and 10 A g^{-1}, separately.

Energy density vs power density Ragone plot of NiCo(1:0.5)MOF H_2O//BAC device were demonstrated in Fig. 8a. The energy densities of the device are 108.96, 76.25, 75.19, 65.73, 57.60, and 53.95 Wh kg^{-1} at 1, 2, 3, 5, 8 and 10 A g^{-1}, with the power densities of 750.00, 1500.00, 2250.00, 3750.00, 6000.00, 7500.00 W kg^{-1}, respectively. The large energy density depends on the higher specific capacitance of NiCo (1:0.5)MOF H_2O and the wide potential window, which is superior to a series of similar device, such as, nano-NiMOF3//AC (13.74 Wh kg^{-1}) [45], rOHNM-AGs//AC (36.40 Wh kg^{-1}) [46], NiCo-LDH@MOF//AC (40.26 Wh kg^{-1}) [47], D-DABA-Ni/Co MOF//AC (85.56 Wh kg^{-1}) [48], Ni-MOF//AC (31.50 Wh kg^{-1}) [49], F-12//AC (24.40 Wh kg^{-1}) [50]. The cycle performance of the device is also studied throughout the 5000 charge-discharge procedure (Fig. 8b). The capacitance retention maintains 89.09 % after 5000 cycles, which is higher than that of Co_9S_8@SNCB//Co_9S_8@SNCB (83.00 %, 2000 cycles) [51], D-DABA--Ni/Co MOF//AC ASC (81.05 %, 5000 cycles) [48], NiCo-23-BDC@MIM

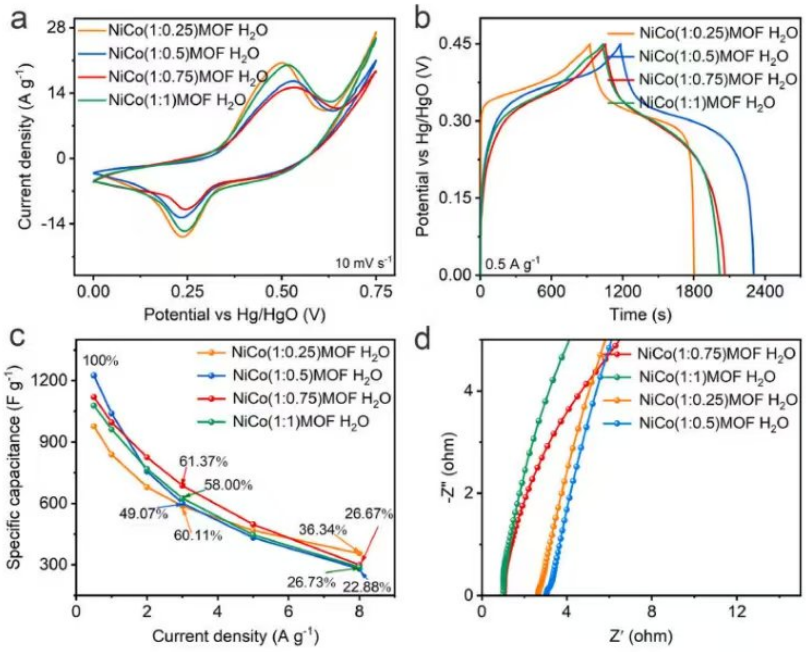

Fig. 6. (a) CV, (b) GCD, (c) rate performance and (d) EIS measurements of NiCo(x:y)MOF H_2O (x:y = 1:0.25, 1:0.5, 1:0.75 and 1:1).

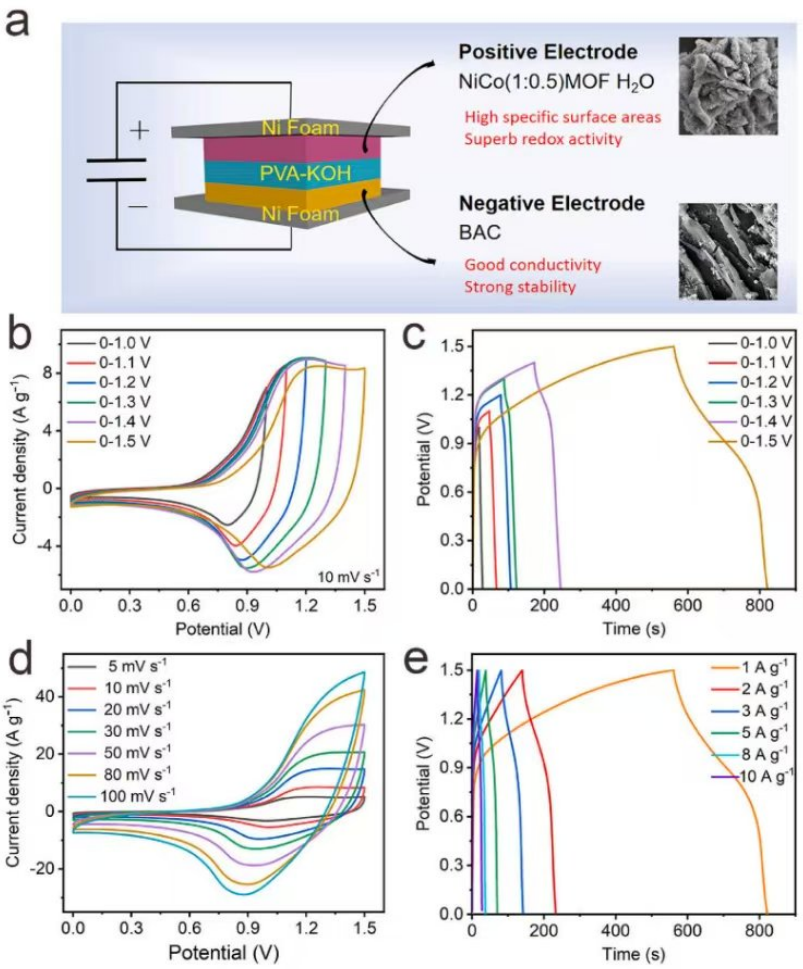

Fig. 7. (a) Hybrid supercapacitor schematic, (b) CV curves and (c) GCD measurement with various potential windows, (d) CV curves at different scan rates, (e) GCD measurement at diverse current densities of NiCo(1:0.5)MOF H_2O//BAC.

(73.20 %, 2000 cycles) [52], Ni-MOF//AC ASC (37.56 %, 5000 cycles) [49], and E-NCT MOF//AC ASC (73.60 %, 10000 cycle) [30]. The good cycling performance depends on both NiCo(1:0.5)MOF H_2O and BAC. Especially, BAC with excellent stability contributes a lot to the whole stability of the device. According to previous reports, NiCo(1:0.5)MOF H_2O tends to generate Ni_xCo_yOH [14]. Therefore, the XRD pattern and XPS spectra of the NiCo(1:0.5)MOF H_2O after cycling are provided in Figs. 8c and S6. The peaks in XRD patterns are attributed to C_2F_4 and Ni, which stem from the adhesive and Ni foam used in the electrode preparation process. No obvious peaks belonged to the NiCo(1:0.5)MOF H_2O after cycling, suggesting the destruction of the original crystal structure. The XPS spectrum (Fig. S6a) after cycling shows the existence of peaks of C, O, Co, Ni, N, and F. The appearance of the peak of F is owing to the binder (C_2F_4). The Co 2p spectrum in Fig. S6b is still divided into four peaks, and the Co $2p_{1/2}$ and Co $2p_{3/2}$ peaks shift a little to the low binding energy compared to the sample before cycling, which indicates a more stable structure. And the Ni 2p peaks (Fig. S6c) attributed to Ni $2p_{1/2}$ and Ni $2p_{3/2}$ show no obvious shift. The C1s (Fig. S6d) spectrum illustrates an extra peak at 292.48 eV, which may belong to the CF_2 group. As observed in O1s spectrum (Fig. S6e), the C–OH bond moves to a higher binding energy, and the peak width of the M−O bond increases, probably as a result of the generation of Ni_xCo_yOH[53, 54]. As shown in Fig. 8d, the devices with good charge storage ability are connected in series, which can support the luminescence of green LED.

4. Conclusions

To sum up, MOFs with various morphology were prepared via a facile solvothermal synthesis under solvent and metal ions effect, which rely on the differences of solvent polarity and solubility as well as the coordination ability of metal ions. Among them, NiCo(1:0.5)MOF H_2O showed the largest specific capacitance of 1225.56 F g^{-1} (specific capacity of 551.50 C g^{-1}) at 0.5 A g^{-1}, which stems from its fine electrochemical activity and highest specific surface area. Based on its superb battery-type behavior, a KOH-activated carbon material derived from bamboo was selected as the anode. The assembled solid-state hybrid supercapacitor delivered an energy density of 108.96 Wh kg^{-1} with a power density of 750.00 W kg^{-1}, exhibited good cycling stability (capacitance retention of 89.09 %, 5000 cycles), and offered enough energy for the luminescence of LED. This work can provide a reference for the application of MOFs in other fields.

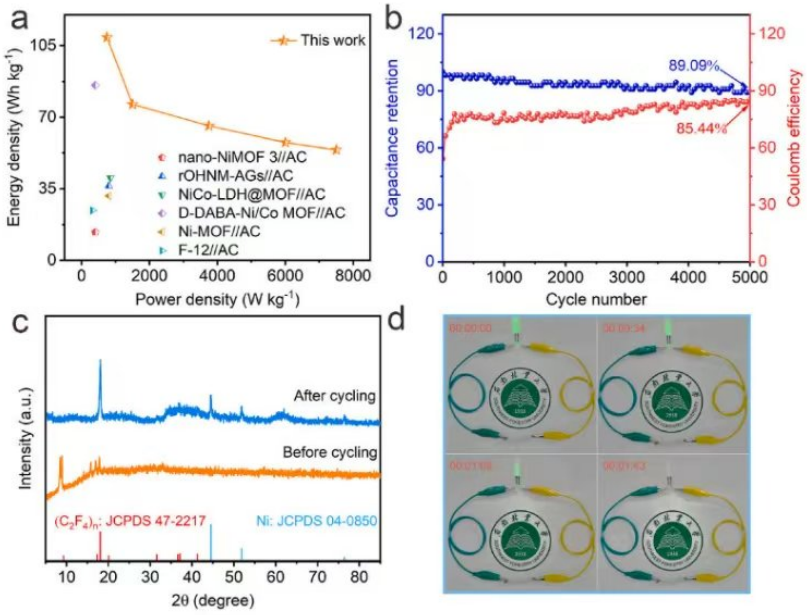

Fig. 8. (a) Energy density vs power density Ragone plot, (b) cycle life and Coulombic efficiency of NiCo(1:0.5)MOF H_2O//BAC, (c) XRD pattern of NiCo(1:0.5)MOF H_2O after cycling, (d) practical circuit diagram.

CRediT authorship contribution statement

Fei Zhou: Writing – original draft, Methodology, Investigation, Formal analysis, Data curation. **Guangjun Liu:** Methodology, Investigation. **Changfu Zhuang:** Validation, Supervision, Project administration, Funding acquisition. **Ying Wang:** Validation, Supervision. **Di Tian:** Writing – review & editing, Writing – original draft, Validation, Project administration, Methodology, Funding acquisition, Formal analysis, Data curation, Conceptualization.

Declaration of competing interest

The authors declare that they have no known competing financial interests or personal relationships that could have appeared to influence the work reported in this paper.

Data availability

Data will be made available on request.

Acknowledgments

This research was funded by the National Natural Science Foundation of China (No.32260368), Yunnan Provincial Support Plan for Xingdian Talent (XDYC-QNRC-2022-0629). Science and Technology Planning Project of Yunnan Province (202201AU 070066, 202101BD070001-052, 202101BD070001-007).

Appendix A. Supplementary data

Supplementary data to this article can be found online at https://doi.org/10.1016/j.mtchem.2024.102198.

References

[1] I.E. Khalil, J. Fonseca, M.R. Reithofer, T. Eder, J.M. Chin, Tackling orientation of metal-organic frameworks (MOFs): the quest to enhance MOF performance, Coord. Chem. Rev. 481 (2023) 215043, https://doi.org/10.1016/j.ccr.2023.215043.
[2] D. Wang, T. Li, Toward MOF@polymer core-shell particles: design principles and potential applications, Acc. Chem. Res. 56 (2023) 462–474, https://doi.org/10.1021/acs.accounts.2c00695.
[3] Y. Liang, X. Yang, X. Wang, Z.-J. Guan, H. Xing, Y. Fang, A cage-on-MOF strategy to coordinatively functionalize mesoporous MOFs for manipulating selectivity in adsorption and catalysis, Nat. Commun. 14 (2023) 5223, https://doi.org/10.1038/s41467-023-40973-9.
[4] N. Huang, Y. Sun, S. Liu, X. Wang, J. Zhang, L. Guo, J. Bi, X. Sun, Microwave-Assisted rational designed cnt-Mn3O4/CoWO4 hybrid nanocomposites for high performance battery-supercapacitor hybrid device, Small 19 (2023) 2300696, https://doi.org/10.1002/smll.202300696.
[5] W. Zuo, R. Li, C. Zhou, Y. Li, J. Xia, J. Liu, Battery-supercapacitor hybrid devices: recent progress and future prospects, Adv. Sci. 4 (2017) 1600539, https://doi.org/10.1002/advs.201600539.
[6] T.-Y. Chen, T.-R. Kuo, S. Yougbaré, L.-Y. Lin, C.-Y. Xiao, Novel direct growth of ZIF-67 derived Co_3O_4 and N-doped carbon composites on carbon cloth as supercapacitor electrodes, J. Colloid Interface Sci. 608 (2022) 493–503, https://doi.org/10.1016/j.jcis.2021.09.198.
[7] H. Pai, T.-R. Kuo, R.-J. Chung, S. Kubendhiran, S. Yougbaré, L.-Y. Lin, Enhanced photocurrent density for photoelectrochemical catalyzing water oxidation using novel W-doped $BiVO_4$ and metal organic framework composites, J. Colloid Interface Sci. 624 (2022) 515–526, https://doi.org/10.1016/j.jcis.2022.05.169.
[8] Y.-F. Wu, T.-R. Kuo, L.-Y. Lin, S. Kubendhiran, K.-C. Lai, T.-Y. Chen, S. Yougbaré, Investigating energy storage ability of MIL101-(Fe) derivatives prepared using successive carbonization and oxidation for supercapacitors, J. Energy Storage 55 (2022) 105420, https://doi.org/10.1016/j.est.2022.105420.
[9] T.-R. Kuo, J.-M. Huang, X.-Y. You, K. Subbiramaniyan, C. Kongvarhodom, M. Saukani, S. Yougbaré, H.-M. Chen, L.-Y. Lin, Facile synthesis of cobalt, nickel and manganese-based metal organic framework derived layered double hydroxides on Ni foam as effective binder-free electrodes of energy storage devices, J. Energy Storage 78 (2024) 110031, https://doi.org/10.1016/j.est.2023.110031.
[10] F. Bi, S. Ma, B. Gao, B. Liu, Y. Huang, R. Qiao, X. Zhang, Boosting toluene deep oxidation by tuning metal-support interaction in MOF-derived $Pd@ZrO_2$ catalysts: the role of interfacial interaction between Pd and ZrO_2, Fuel 357 (2024) 129833, https://doi.org/10.1016/j.fuel.2023.129833.
[11] S. Ma, W. Han, W. Han, F. Dong, Z. Tang, Recent advances and future perspectives in MOF-derived single-atom catalysts and their application: a review, J. Mater. Chem. A 11 (2023) 3315–3363, https://doi.org/10.1039/d2ta08735a.
[12] Y. Fu, L. Zhang, Y. Li, S. Guo, Z. Yu, W. Wang, K. Ren, Q. Peng, S. Han, Catalytic effect of MOF-derived transition metal catalyst FeCoS@C on hydrogen storage of magnesium, J. Mater. Sci. Technol. 138 (2023) 59–69, https://doi.org/10.1016/j.jmst.2022.08.019.

[13] L. Kong, Z. Yuan, H. Gao, F. Meng, Recent progress of gas sensors based on metal oxide composites derived from bimetallic metal-organic frameworks, TrAC, Trends Anal. Chem. 166 (2023) 117199, https://doi.org/10.1016/j.trac.2023.117199.

[14] D. Tian, N. Song, M. Zhong, X. Lu, C. Wang, Bimetallic MOF nanosheets decorated on electrospun nanofibers for high-performance asymmetric supercapacitors, ACS Appl. Mater. Interfaces 12 (2019) 1280–1291, https://doi.org/10.1021/acsami.9b16420.

[15] C. Wang, X. Li, W. Yang, Y. Xu, H. Pang, Solvent regulation strategy of Co-MOF-74 microflower for supercapacitors, Chin. Chem. Lett. 32 (2021) 2909–2913, https://doi.org/10.1016/j.cclet.2021.04.017.

[16] M.A. Molina, N.R. Habib, I. Díaz, M. Sánchez-Sánchez, Surfactant-induced hierarchically porous MOF-based catalysts prepared under sustainable conditions and their ability to remove bisphenol A from aqueous solutions, Catal. Today 394–396 (2022) 117–124, https://doi.org/10.1016/j.cattod.2021.10.019.

[17] L. Huelsenbeck, H. Luo, P. Verma, J. Dane, R. Ho, E. Beyer, H. Hall, G.M. Geise, G. Giri, Generalized approach for rapid aqueous MOF synthesis by controlling solution pH, Cryst. Growth Des. 20 (2020) 6787–6795, https://doi.org/10.1021/acs.cgd.0c00895.

[18] J. Liu, T.A. Goetjen, Q. Wang, J.G. Knapp, M.C. Wasson, Y. Yang, Z.H. Syed, M. Delferro, J.M. Notestein, O.K. Farha, J.T. Hupp, MOF-enabled confinement and related effects for chemical catalyst presentation and utilization, Chem. Soc. Rev. 51 (2022) 1045–1097, https://doi.org/10.1039/d1cs00968k.

[19] B. Yu, T. Meng, X. Ding, X. Liu, H. Wang, B. Chen, T. Zheng, W. Li, Q. Zeng, J. Jiang, Hydrogen-bonded organic framework ultrathin nanosheets for efficient visible-light photocatalytic CO_2 reduction, Angew. Chem. Int. Ed. 61 (2022) e202211482, https://doi.org/10.1002/anie.202211482.

[20] R. Seetharaj, P.V. Vandana, P. Arya, S. Mathew, Dependence of solvents, pH, molar ratio and temperature in tuning metal organic framework architecture, Arab. J. Chem. 12 (2019) 295–315, https://doi.org/10.1016/j.arabjc.2016.01.003.

[21] N. Stock, S. Biswas, Synthesis of metal-organic frameworks (MOFs): routes to various MOF topologies, morphologies, and composites, Chem. Rev. 112 (2011) 933–969, https://doi.org/10.1021/cr200304e.

[22] A.G. Zavyalova, D.V. Kladko, I.Y. Chernyshov, V.V. Vinogradov, Large MOFs: synthesis strategies and applications where size matters, J. Mater. Chem. 9 (2021) 25258–25271, https://doi.org/10.1039/d1ta05283g.

[23] J. Sun, X. Yu, S. Zhao, H. Chen, K. Tao, L. Han, Solvent-controlled morphology of amino-functionalized bimetal metal-organic frameworks for asymmetric supercapacitors, Inorg. Chem. 59 (2020) 11385–11395, https://doi.org/10.1021/acs.inorgchem.0c01157.

[24] J. Hwang, R. Yan, M. Oschatz, B.V.K.J. Schmidt, Solvent mediated morphology control of zinc MOFs as carbon templates for application in supercapacitors, J. Mater. Chem. A 6 (2018) 23521–23530, https://doi.org/10.1039/c8ta07700b.

[25] C.-H. Wang, D.-W. Zhang, S. Liu, Y. Yamauchi, F.-B. Zhang, Y.V. Kaneti, Ultrathin nanosheet-assembled nickel-based metal-organic framework microflowers for supercapacitor applications, Chem. Commun. 58 (2022) 1009–1012, https://doi.org/10.1039/d1cc04880e.

[26] A. Khan, S.M. Sapuan, J. Yusuf, V.U. Siddiqui, E.S. Zainudin, M.Y.M. Zuhri, B.T. H. Tuah Baharuddin, M.A. Ansari, A.A.A. Rahman, An examination of cutting-edge developments in Bamboo-PLA composite research: a comprehensive review, Renewable Sustainable Energy Rev. 188 (2023), https://doi.org/10.1016/j.rser.2023.113832.

[27] M. Song, D. Kim, S. Jeon, Bamboo-alginate composite as a sustainable structural material, ACS Sustainable Chem. Eng. 11 (2023) 3486–3493, https://doi.org/10.1021/acssuschemeng.2c07232.

[28] H. Wei, S. Deng, B. Hu, Z. Chen, B. Wang, J. Huang, G. Yu, Granular bamboo-derived activated carbon for high CO_2 adsorption: the dominant role of narrow micropores, ChemSusChem 5 (2012) 2354–2360, https://doi.org/10.1002/cssc.201200570.

[29] Y.-J. Kim, B.-J. Lee, H. Suezaki, T. Chino, Y. Abe, T. Yanagiura, K.C. Park, M. Endo, Preparation and characterization of bamboo-based activated carbons as electrode materials for electric double layer capacitors, Carbon 44 (2006) 1592–1595, https://doi.org/10.1016/j.carbon.2006.02.011.

[30] S. Song, X. Ma, B. Zhang, W. Li, Y. Feng, C. Tan, Morphologies of thienyl based bimetallic metal-organic frameworks controlled by solvents for high specific capacitance supercapacitor, J. Energy Storage 47 (2022) 103627, https://doi.org/10.1016/j.est.2021.103627.

[31] R. Ramachandran, C. Zhao, D. Luo, K. Wang, F. Wang, Morphology-dependent electrochemical properties of cobalt-based metal organic frameworks for supercapacitor electrode materials, Electrochim. Acta 267 (2018) 170–180, https://doi.org/10.1016/j.electacta.2018.02.074.

[32] S. Qiang Zheng, S. Shee Lim, C. Yi Foo, C. Yian Haw, W. Siong Chiu, C. Hua Chia, P. Sim Khiew, Probing the effect of solvents on the electrochemical performance of graphene incorporated nickel-based metal organic frameworks, J. Electroanal. Chem. 925 (2022) 116860, https://doi.org/10.1016/j.jelechem.2022.116860.

[33] M.J. Van Vleet, T. Weng, X. Li, J.R. Schmidt, In situ, time-resolved, and mechanistic studies of metal-organic framework nucleation and growth, Chem. Rev. 118 (2018) 3681–3721, https://doi.org/10.1021/acs.chemrev.7b00582.

[34] D. Tian, X. Lu, Y. Zhu, M. Li, C. Wang, Fabrication of two-dimensional metal-organic frameworks on electrospun nanofibers and their derived metal doped carbon nanofibers for an advanced asymmetric supercapacitor with a high energy density, J. Power Sources 413 (2019) 50–58, https://doi.org/10.1016/j.jpowsour.2018.12.014.

[35] A. Mesbah, P. Rabu, R. Sibille, S. Lebègue, T. Mazet, B. Malaman, M. François, From hydrated $Ni_3(OH)_2(C_8H_4O_4)_2(H_2O)_4$ to anhydrous $Ni_2(OH)_2(C_8H_4O_4)$: impact of structural transformations on magnetic properties, Inorg. Chem. 53 (2014) 872–881, https://doi.org/10.1021/ic402106v.

[36] W. Wu, C. Wu, G. Zhang, J. Liu, Y. Li, G. Li, Synthesis and characterization of magnetic K_2CO_3-activated carbon produced from bamboo shoot for the adsorption of Rhodamine b and CO2 capture, Fuel 332 (2023) 126107, https://doi.org/10.1016/j.fuel.2022.126107.

[37] Y. Jiao, J. Pei, C. Yan, D. Chen, Y. Hu, G. Chen, Layered nickel metal-organic framework for high performance alkaline battery-supercapacitor hybrid devices, J. Mater. Chem. A 4 (2016) 13344–13351, https://doi.org/10.1039/c6ta05384j.

[38] A. Carton, A. Mesbah, T. Mazet, F. Porcher, M. François, Ab initio crystal structure of nickel(II) hydroxy-terephthalate by synchrotron powder diffraction and magnetic study, Solid State Sci. 9 (2007) 465–471, https://doi.org/10.1016/j.solidstatesciences.2007.04.003.

[39] Y. Cao, N. Wu, C. Li, Y. Chen, H. Zhang, H. Guo, W. Yang, Solvent-regulated synthesis and phosphating of nickel-cobalt bimetal organic framework microflowers with hierarchical structure for high-performance supercapacitors, Colloids Surf., A 658 (2023) 130683, https://doi.org/10.1016/j.colsurfa.2022.130683.

[40] Y. Wang, Y. Liu, H. Wang, W. Liu, Y. Li, J. Zhang, H. Hou, J. Yang, Ultrathin NiCo-MOF nanosheets for high-performance supercapacitor electrodes, ACS Appl. Energy Mater. 2 (2019) 2063–2071, https://doi.org/10.1021/acsaem.8b02128.

[41] Q. Chen, S. Lei, P. Deng, X. Ou, L. Chen, W. Wang, Y. Xiao, B. Cheng, Direct growth of nickel terephthalate on Ni foam with large mass-loading for high-performance supercapacitors, J. Mater. Chem. A 5 (2017) 19323–19332, https://doi.org/10.1039/c7ta05373h.

[42] X. Shi, L. Sun, X. Li, L. Wu, J. Qian, J. Wang, Y. Lin, S. Su, C. Sun, Y. Zhang, Y. Zhang, High-performance flexible supercapacitor enabled by Polypyrrole-coated NiCoP@CNT electrode for wearable devices, J. Colloid Interface Sci. 606 (2022) 135–147, https://doi.org/10.1016/j.jcis.2021.08.016.

[43] J. Wang, X. Ma, Z. Zhu, K. Fang, N. Wang, C. Wang, G. Nie, Pore engineering in robust carbon nanofibers for highly efficient capacitive deionization, Sep. Purif. Technol. 332 (2024) 125797, https://doi.org/10.1016/j.seppur.2023.125797.

[44] G. Liu, K. Yan, F. Zhou, Y. Wang, C. Zhuang, C. Wang, D. Tian, Fabrication of hierarchical Co doped Ni_3Se_4 on ZIF-67 modified carbon nanofibers for high-performance hybrid supercapacitors, Electrochim. Acta 464 (2023) 142922, https://doi.org/10.1016/j.electacta.2023.142922.

[45] M. Gu, M. Wu, S.-C. Wang, C. Chen, D. Xiong, F.-Y. Yi, Morphology control of nanoscale metal-organic frameworks for high-performance supercapacitors, Electrochim. Acta 343 (2020) 135617, https://doi.org/10.1016/j.electacta.2020.135617.

[46] H. Zong, A. Zhang, J. Dong, Y. He, H. Fu, H. Guo, F. Liu, J. Xu, J. Liu, Flexible asymmetric supercapacitor based on Open-Hollow Nickel-MOFs/Reduced graphene oxide aerogel electrodes, Chem. Eng. J. 475 (2023) 146088, https://doi.org/10.1016/j.cej.2023.146088.

[47] C. Shi, Y. Du, L. Guo, J. Yang, Y. Wang, Construction of interconnected NiCo layered double hydroxides/metal-organic frameworks hybrid nanosheets for high-performance supercapacitor, J. Energy Storage 48 (2022) 103961, https://doi.org/10.1016/j.est.2022.103961.

[48] S. Song, X. Ma, W. Li, B. Zhang, J. Sun, C. Deng, The influence of solvent controlled morphology on capacitive properties of metal-organic frameworks based on polyaminocarboxybenzene ligands, Colloids Surf., A 656 (2023) 130350, https://doi.org/10.1016/j.colsurfa.2022.130350.

[49] S. Gao, Y. Sui, F. Wei, J. Qi, Q. Meng, Y. He, Facile synthesis of cuboid Ni-MOF for high-performance supercapacitors, J. Mater. Sci. 53 (2018) 6807–6818, https://doi.org/10.1007/s10853-018-2005-1.

[50] X. Chen, C. Wang, Y. Wang, J. Ma, Y. Dong, S. Gao, Q. Jing, W. Li, H. Pang, In-situ immobilization cobalt-based metal-organic frameworks nanosheets on carbon composites for supercapacitors, J. Energy Storage 55 (2022) 105319, https://doi.org/10.1016/j.est.2022.105319.

[51] S. Liu, M. Tong, G. Liu, X. Zhang, Z. Wang, G. Wang, W. Cai, H. Zhang, H. Zhao, S, N-Containing Co-MOF derived Co_9S_8@S,N-doped carbon materials as efficient oxygen electrocatalysts and supercapacitor electrode materials, Inorg. Chem. Front. 4 (2017) 491–498, https://doi.org/10.1039/c6qi00403b.

[52] S.Y. Lee, H.J. An, J. Moon, D.H. Kim, K.W. Park, J.T. Park, Design of ultra-thin nanosheet bimetallic NiCo MOF with binary ligand via solvent-assisted ligand exchange (SALE) reaction for high performance supercapacitors, Electrochim. Acta 451 (2023) 142291, https://doi.org/10.1016/j.electacta.2023.142291.

[53] X. Xu, J. Yang, Y. Hong, J. Wang, Nitrate precursor driven high performance Ni/Co-MOF nanosheets for supercapacitors, ACS Appl. Nano Mater. 5 (2022) 8382–8392, https://doi.org/10.1021/acsanm.2c01488.

[54] M. Zhong, J. Yang, M. Xu, S. Ren, X. Chen, C. Wang, M. Gao, X. Lu, Significantly enhanced energy-saving H_2 production coupled with urea oxidation by low- and non-Pt anchored on NiS-based conductive nanofibers, Small 20 (2023) 2304782, https://doi.org/10.1002/smll.202304782.